

A crucial role of surface oxygen mobility on nanocrystalline Y_2O_3 support for oxidative steam reforming of ethanol to hydrogen over $\text{Ni}/\text{Y}_2\text{O}_3$ catalysts

G.B. Sun, K. Hidajat, X.S. Wu, S. Kawi*

Department of Chemical and Biomolecular Engineering, National University of Singapore, 4 Engineering Drive 4, Singapore 119260, Singapore

Received 27 November 2006; received in revised form 12 December 2007; accepted 16 December 2007

Available online 3 January 2008

Abstract

Y_2O_3 nanocrystals hydrothermally synthesized at different pH are found to have different morphologies and crystal sizes. These Y_2O_3 nanocrystals have been investigated as supports of Ni-based catalysts in oxidative reforming reaction of ethanol. Result of H_2 -chemisorption shows that the particle size and dispersion of nickel on Y_2O_3 nanocrystals are not affected significantly by the crystal size of Y_2O_3 . XPS and H_2 -TPR results show that no association between nickel and the support- Y_2O_3 has taken place and the reducibility of nickel is not affected by the crystal size of Y_2O_3 . However, it is found that the surface oxygen mobility of Y_2O_3 nanocrystal increases with decreasing crystal size. The surface oxygen mobility is believed to play an important role in promoting the H_2 production rate and selectivity of the $\text{Ni}/\text{Y}_2\text{O}_3$ catalyst over the oxidative steam reforming of ethanol.

© 2008 Elsevier B.V. All rights reserved.

Keywords: Nickel; Yttrium oxide; Surface oxygen mobility; Ethanol reforming; Hydrogen

1. Introduction

The ever-increasing demand for H_2 as a green energy carrier or chemical in a variety of industries has promoted intense research interests in H_2 production [1–3], purification [4–6], storage [7] and utilization [8]. Reforming of hydrocarbons and alcohols is an important route for hydrogen production and hence an active area of catalysis research [9]. Compared with hydrocarbons, alcohol requires milder reforming conditions and it is therefore considered to be one of the most promising fuels for producing hydrogen on-board for specific applications, such as, mobile fuel cell devices [10]. Among the various alcoholic fuels, ethanol is a very attractive fuel since it can be produced from the fermentation of biomass [11,12]. The bioethanol-to-hydrogen system is nearly CO_2 neutral with carbon circulating in a closed loop as the carbon dioxide produced can be consumed for biomass growth [13]. Furthermore, the storage, transportation and distribution of ethanol are rather safe and easy [14]. Therefore, research on H_2

production from ethanol has been gaining increasing attention in recent years [15].

A variety of metals, such as Co, Ni, Cu, Rh, Pd, Pt, etc. [16–25], have been shown to be active for ethanol reforming. Among these metals, Ni is especially attractive due to its high activity and low cost [26,27]. Hence, many oxides such as Al_2O_3 , SiO_2 , MgO , ZnO , La_2O_3 , CeO_2 and Y_2O_3 have been investigated as the support for nickel metal catalyst in order to obtain a high performance catalyst for efficiently producing hydrogen from ethanol reforming [13,17,26–29]. It has been found that Ni supported on some oxides, such as Y_2O_3 shows better performance than that on other oxides, such as Al_2O_3 [30,31]. However, it is still not fully understood yet how the support influences the performance of a supported metal catalyst for ethanol reforming.

For a supported metal catalyst, it has been well established that factors, such as the specific surface area, dispersion and particle size of the supported metal influence the performance of the catalyst [32–34]. Recently, the structure and crystal size of catalyst support have also been found to play important roles in a variety of reaction systems. For instance, Guzman and Corma [35] have found that nanocrystalline Y_2O_3 can stabilize more active species of gold than mesostructured Y_2O_3 and

* Corresponding author. Tel.: +65 65166312; fax: +65 67791936.

E-mail address: chekawis@nus.edu.sg (S. Kawi).

hence enhances the activity of gold catalyst in CO selective oxidation reaction. While Kugai et al. [36] have investigated the effects of nanocrystalline CeO_2 supports and found that Ni-Rh catalyst supported on smaller CeO_2 nanocrystals shows better performance in oxidative steam reforming of ethanol. These valuable findings provide an important clue to reveal the role of catalyst support on the performance of metal supported catalysts.

Further studies in this area are needed in order to obtain comprehensive understanding of the role of supports on the performance of metal supported catalysts. In the present study, four different crystal sizes of Y_2O_3 supports have been successfully synthesized and investigated as the supports of Ni-based catalysts for oxidative steam reforming of ethanol. The influence of Y_2O_3 crystal size on the catalytic performance of Ni/ Y_2O_3 is examined. The changes of the properties of both the active ingredient and the support with the variation of the crystal size of Y_2O_3 are also investigated in order to gain a fundamental understanding on the role of nanocrystalline support in oxidative reforming reaction.

2. Experimental

2.1. Support synthesis and catalyst preparation

Y_2O_3 samples were hydrothermally synthesized under different pH. A typical synthesis of Y_2O_3 is as follows: 7.66 g of $\text{Y}(\text{NO}_3)_3 \cdot 6\text{H}_2\text{O}$ (Aldrich) was dissolved in 100 ml of deionized (DI) water at room temperature. A desired amount of aqueous ammonia (10%) was slowly added to the yttrium nitrate solution to control the solution pH at 7, 9, 11 or 12. The resultant opaque slurry with white precipitate was obtained and transferred to a Teflon-lined stainless steel autoclave. This autoclave was sealed and placed in a thermostatic oven and hydrothermally treated at 170 °C for 20 h. The solid material was recovered by centrifuging, washing with DI water for several times and drying at 100 °C overnight. Finally, Y_2O_3 was obtained after calcination in air at 800 °C for 5 h using a heating rate of 5 °C/min. These four Y_2O_3 samples synthesized at pH 7, 9, 11 and 12 are designated as Y7, Y9, Y11 and Y12, respectively.

Ni/ Y_2O_3 catalysts were prepared by wet impregnation method. Typically, 1.4 g of Y_2O_3 (either Y7, Y9, Y11 or Y12) was added to a solution of 0.3 g of $\text{Ni}(\text{NO}_3)_2 \cdot 6\text{H}_2\text{O}$ (Merck) in 40 ml of DI water with vigorous stirring at room temperature for 2 h. Finally, this mixture was thoroughly dried at 100 °C followed by calcination in air at 600 °C for 5 h. The resultant four catalysts are designated as Ni/Y7, Ni/Y9, Ni/Y11 and Ni/Y12, respectively.

2.2. Support and catalyst characterizations

The morphology of Y_2O_3 samples was visually observed using a field emission scanning electron microscope (FESEM: Jeol JSM-6700F). The nickel particles impregnated on the surface of Y_2O_3 were observed using a transmission electron microscope (TEM: Jeol JEM-2010). N_2 adsorption–desorption isotherms were measured by nitrogen physisorption at 77 K

using Autosorb-1 (Quantachrome) system. Prior to nitrogen adsorption–desorption measurements, the samples were degassed at 300 °C under vacuum for 2 h. The specific surface areas of catalysts were determined from the linear portion of BET plots. The powder X-ray diffraction (XRD) patterns of samples were recorded using a Shimadzu XRD-6000 powder diffractometer, where Cu target $\text{K}\alpha$ -ray (operating at 40 kV and 30 mA) was used as the X-ray source. ICP analysis was also conducted in order to measure the content of Ni in each catalyst.

X-ray photoelectron spectroscopy (XPS) was performed on a Kratos AXIS. His spectrometer using a monochromatized Al $\text{K}\alpha$ X-ray source (1486.6 eV photons) at a constant dwell time of 100 ms and pass energy of 40 eV. The sample was mounted on the standard sample stubs using double-sided adhesive tapes. The core level signals were obtained at a photoelectron takeoff angle (R , measured with respect to the sample surface) of 90°. The X-ray source was run at a reduced power of 150 W (15 kV and 10 mA). The pressure in the analysis chamber was maintained at 10^{-8} Torr or lower during each measurement. All binding energies were referenced to the C 1s hydrocarbon peak at 284.6 eV.

Temperature-programmed reduction (TPR) experiments were performed using Quantachrome ChemBET 3000 TPD/TPR system equipped with a thermal conductivity detector (TCD). 50 mg of sample (either Y_2O_3 support or catalyst) was first degassed at 350 °C for 1 h with dry air flushing. Then, 5% H_2/N_2 gas mixture at a flow rate of 80 ml/min was passed through the sample and TPR profiles were obtained by heating the sample from sub-ambient temperature to 800 °C at a heating rate of 10 °C/min. The effluent gas was passed through a cold trap in order to remove the water produced. The output signal of the dried gas mixture as a function of temperature was continuously monitored using the TCD and was recorded by a microcomputer. The amount of H_2 consumed during H_2 -TPR of Y_2O_3 is calculated based on the peak area of TPR profile.

Hydrogen chemisorption and temperature-programmed desorption (H_2 -TPD) were also performed with the above-mentioned TPD/TPR system in order to determine the dispersion and particle size of nickel in the catalyst. 50 mg of catalyst was initially reduced at 450 °C for 2 h followed by H_2 adsorption at 30 °C for 60 min. After removing all the physically adsorbed H_2 with N_2 flow, H_2 -TPD was conducted from 30 to 600 °C. H_2 pulse titration was also performed at 30 °C with the same system. The amount of surface nickel atoms was calculated from the amount of desorbed H_2 , assuming a stoichiometry of one hydrogen molecule adsorbed per two surface nickel atoms. The nickel dispersion is calculated as the percentage of surface nickel atoms with respect to total nickel atoms in the catalysts. The particle size of nickel is calculated based on the H_2 -TPD profiles and hydrogen titration experiment.

2.3. Activity test

Catalytic reactions were carried out in a micro-catalytic reactor (O.D. 1/4 in.) using a single pass, steady-state plug flow mode. The catalysts were crushed and sieved to 0.250–0.425 mm before loading to the reactor. The temperature of the

catalyst bed was controlled and monitored by a thermocouple that was in contact with the top layer of the catalyst bed. Before testing, the catalyst was reduced under flowing pure hydrogen (10 ml/min) at 450 °C for 30 min. A liquid water/ethanol mixture was first fed into a preheater (set at 150 °C) using syringe pump. The vapor was carried into the reactor with nitrogen flowing at 30 ml/min. Oxygen was separately fed with an independent mass flow controller. Typically, 100 mg of catalyst was used for each test and the gas mixture reactants of ethanol/water/oxygen (having a molar ratio of 1:3:0.5) were fed with a space velocity of 44,170 h⁻¹. Tests were performed from 500 to 750 °C and atmospheric pressure. The reactor effluent went through a condenser to trap condensable vapors (ethanol, water, acetaldehyde etc.). The gas product was analyzed using a gas chromatograph (HP 6890) equipped with a Porapak Q, a molecular sieve 5 A column and a TCD detector. The liquid product was analyzed separately by a gas chromatograph equipped with INNOWax capillary column and FID detector.

In order to measure the amount of carbon deposit during the catalytic test, thermogravimetric analysis (TGA) of the used catalyst samples was performed on a Shimadzu DTG-60 thermogravimetric analyzer. Around 15 mg of sample was used in each TGA experiment and the sample was heated in air to 800 °C with a heating rate of 10 °C/min.

3. Results and discussion

3.1. Characterizations on Y₂O₃ supports

FESEM images (Fig. 1) show that the synthesis pH affects the morphology of the resultant Y₂O₃. The Y₂O₃ synthesized at pH 7 has sheet-like shape, with a thickness of about 200 nm and

irregular sizes. When the pH is adjusted to 9, the resultant Y₂O₃ particles have hexagonal prism morphology, with a diameter of around 2 μm and length of up to several micrometers. With a further increase of pH to 11, Y₂O₃ has nanorod-like structure with a diameter around 100 nm. However, when the pH is adjusted to 12, the resultant Y₂O₃ has nanosheet-like shape with much thinner thickness of only about 10 nm. These Y₂O₃ nanosheets have been found to be thermally stable as they are not sintered together even after being thermally treated at 800 °C for 10 h. Zhang et al. [37] reported the synthesis of prism-shaped Y₂O₃ at 200 °C using ammonia as the precipitating agent, but they did not observe any morphology change despite the change of synthesis pH from 8 to 11; this is probably because higher hydrothermal temperature (200 °C) and higher solution concentration were used in their synthesis, which might restrain the morphology change. It is well known that factors such as pH, hydrothermal temperature and solution concentration could significantly affect the anisotropic growth of materials [38]. Wang et al. [38,39] have reported the synthesis of Y₂O₃ nanotube at around 130 °C and a mixture of nanorod, nanotube and nanosheet at around 180 °C using NaOH as the precipitating agent. Besides, Guzman and Corma [35] have reported the synthesis of mesostructured Y₂O₃. However, to our knowledge, this is the first report of the synthesis of uniform and stable nanosheet-like Y₂O₃ particles.

The crystal structures of these Y₂O₃ samples differing in morphology are characterized with XRD. It is observed from the XRD patterns (Fig. 2) that the diffraction peaks of (2 1 1), (2 2 2), (4 0 0), (4 4 0) and (6 2 2) are clearly distinguishable, and all of them can be perfectly indexed to the cubic phase (according to JCPDS 25-1200), indicating that the crystal structures of these Y₂O₃ samples are similar despite of their

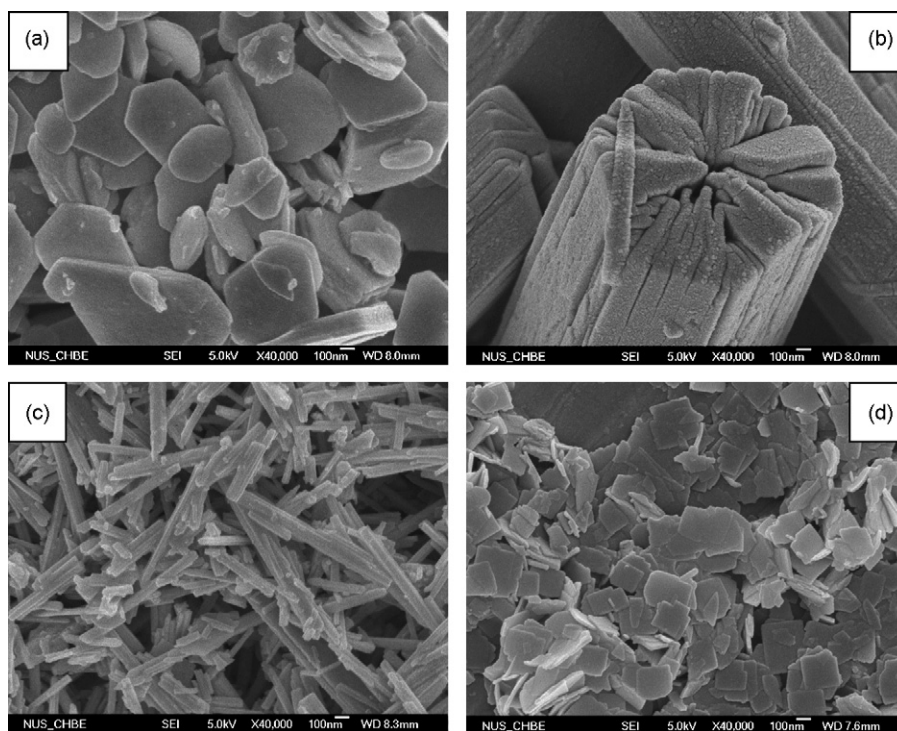


Fig. 1. FESEM images of Y₂O₃ synthesized at pH of: (a) 7; (b) 9; (c) 11; (d) 12.

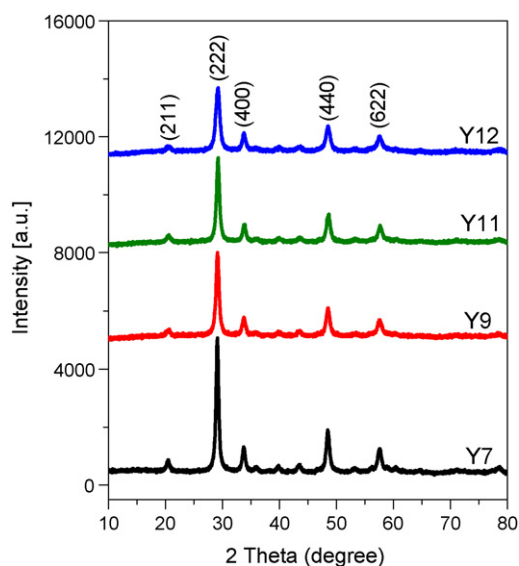


Fig. 2. XRD patterns of Y_2O_3 particles synthesized at different pH.

different morphologies. It can also be observed from Fig. 2 that Y7 gives the sharpest XRD peaks while Y12 exhibits the broadest, indicating that the Y_2O_3 crystals synthesized under near-neutral condition (i.e. at pH 7) are larger than those synthesized under basic condition. The crystal sizes of these Y_2O_3 -samples, which are calculated with Debye–Scherrer formula [40] and listed in Table 1, are around 38, 25, 19 and 9 nm for Y7, Y9, Y11 and Y12, respectively.

The H_2 -TPR profiles in Fig. 3 show that yttrium oxides can be reduced at temperature above 500 °C. The theoretical hydrogen consumption for complete reduction of Y_2O_3 is 13.3 mmole/g. However, the actual H_2 consumption (see Table 1) is only corresponding to a reduction degree of around 1% or less. This result indicates that yttrium oxide can only be partially reduced at the temperature range of 500–800 °C. A similar finding has been reported by Passos et al. [41]. Although, the exact reason of the partial reduction has not been identified yet, the most probable explanation is that hydrogen molecules can only consume the oxygen located on the surface of Y_2O_3 , and hence the position and intensity of the H_2 consumption peaks could be used to indicate the surface oxygen mobility of these yttrium oxides. Similar method has been used to indicate the mobility of surface oxygen on other oxides, such as CeO_2 [42,43]. Comparing the TPR profiles of these Y_2O_3 , it can be seen that the maximum peak height of Y7 appears at the highest temperature (around 700 °C) while that

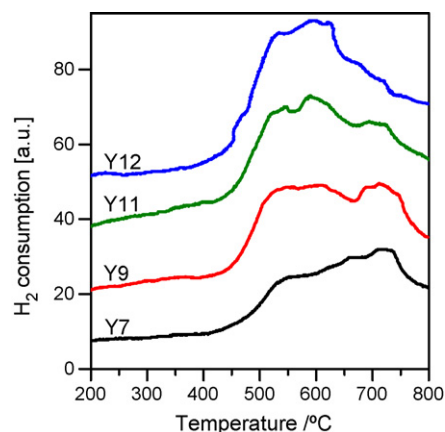


Fig. 3. TPR profiles of Y_2O_3 particles synthesized at different pH.

of Y12 appears at the lowest (around 600 °C), indicating that the surface oxygen species become more and more active from Y7 to Y12. This result implies that the surface oxygen mobility increases from Y7 to Y12 since the lower the temperature at which the reduction peak appears the higher oxidizing ability/oxygen mobility an oxide exhibits [42]. This increase in the surface oxygen mobility of Y_2O_3 should be attributed to the decrease in the crystal size because the smaller the crystal, the higher the surface energy and hence a larger amount of surface oxygen species can be reduced at lower temperature (around 500–650 °C). It can be seen from Table 1 that the consumption amount of H_2 also varies from 86 $\mu\text{mole/g}$ for Y7 to 149 $\mu\text{mole/g}$ for Y12, suggesting that the available amount of mobile oxygen species on the surface of Y12 is larger than that of Y7 in this temperature range. For a partially reducible oxide, the amount of mobile oxygen species could be significantly affected by the amount of the interstitial oxygen ions because it has been reported that the mobile oxygen species in an oxide crystal are provided by the interstitial oxygen ions [43]. It is believed that the amount of crystalline defects of an oxide is closely related to the concentration of the interstitial oxygen [43] i.e. the more crystalline defects an oxide possesses, the larger amount of interstitial oxide it has. Therefore, it is likely that Y12, which has the smallest crystal size, should have the largest amount of crystalline defects and hence the largest amount of mobile oxygen species. On the other hand, either Y7, Y9, or Y11, which has larger crystal size than Y12, should have more perfect crystalline structure with fewer defects and hence smaller amount of mobile surface oxygen species than Y12. This observation explains why the amount of mobile surface oxygen species increases with the decrease of crystal size.

Table 1
Textural characterizations of Y_2O_3 particles synthesized at different pH

Sample	Synthesis pH	Crystal size (nm) ^a	S_{BET} (m^2/g)	H_2 consumption ($\mu\text{mole/g}$) ^b
Y7	7	38	25	86
Y9	9	25	22	101
Y11	11	19	28	123
Y12	12	9	43	149

^a Calculated using Debye–Scherrer formula.

^b Calculated from H_2 -TPR profile up to 800 °C.

3.2. Characterizations on $\text{Ni}/\text{Y}_2\text{O}_3$ catalysts

Fig. 4 shows the morphologies of the calcined catalysts. It can be seen clearly that the presence of NiO particles on the surface of Y_2O_3 supports makes the surface of Y_2O_3 particles less smooth than that of the fresh Y_2O_3 particles. It can also be seen that the particle sizes of NiO on all the four catalysts are comparable (around 15 nm), indicating that crystal sizes of

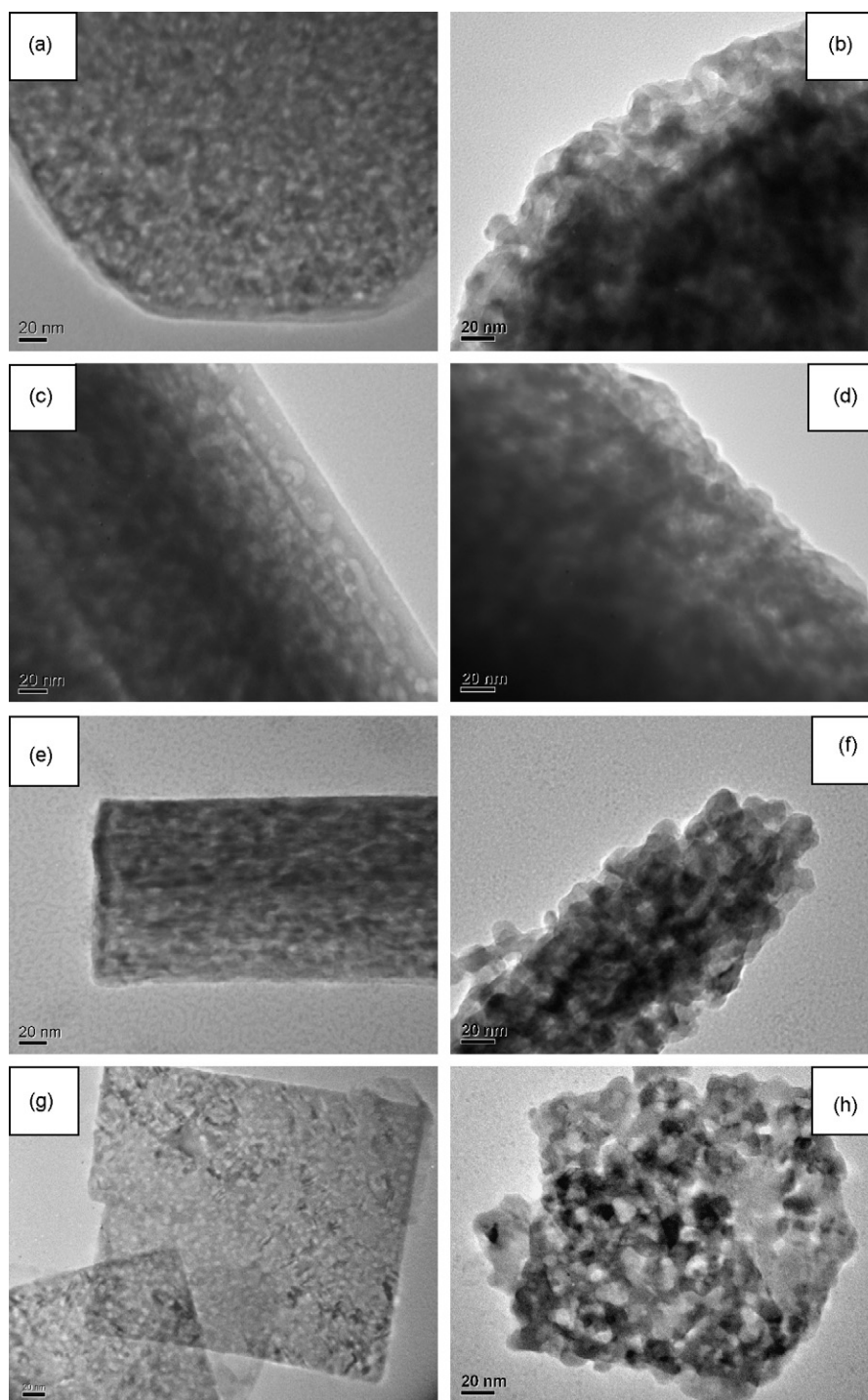


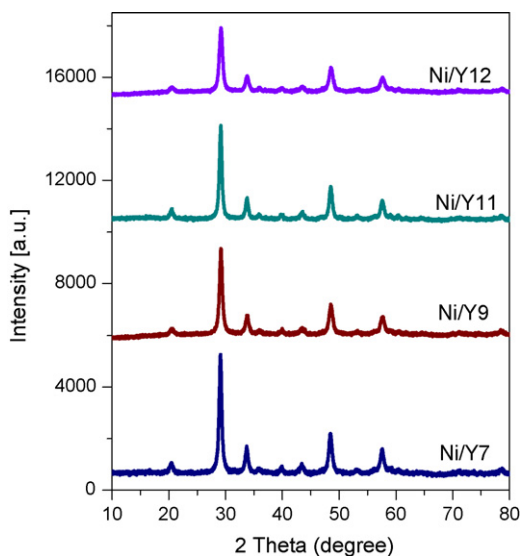
Fig. 4. TEM images of: (a) Y7; (b) Ni/Y7; (c) Y9; (d) Ni/Y9; (e) Y11; (f) Ni/Y11; (g) Y12; (h) Ni/Y12 (Scale bar = 20 nm).

Y_2O_3 supports do not significantly affect the particle size of the impregnated NiO.

Comparing the XRD patterns of $\text{Ni}/\text{Y}_2\text{O}_3$ catalysts (Fig. 5) with those of Y_2O_3 supports (Fig. 2), no distinguishable peaks indexed to NiO can be observed, indicating that almost no detectable NiO crystals exist in these catalysts. This result indicates that nickel can be uniformly and finely dispersed onto Y_2O_3 supports using wet impregnation method.

Fig. 6a shows the Ni 2p XPS spectra of the calcined catalysts. The calcined catalysts exhibit Ni 2p_{3/2} main peak at

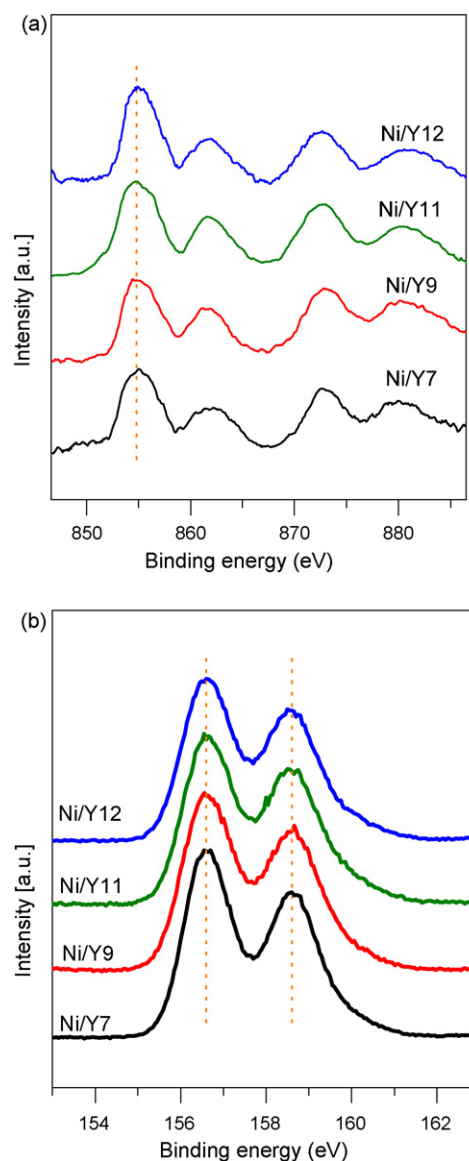
854.4 ± 0.2 eV with a satellite peak around 861.0 eV and Ni 2p_{1/2} main peak at 872.4 ± 0.2 eV with a satellite peak around 880.0 eV, showing that the Ni in the calcined catalysts is essentially in Ni^{2+} oxidation state [44,45]. It is also noted that the measured Ni 2p_{3/2} binding energy perfectly fits with the standard Ni 2p_{3/2} binding energy of the pure NiO (854.5 eV), indicating that no complex oxides/spinel exists therein [45]. This result shows that no association between the Ni and the support Y_2O_3 has taken place during the process of impregnation and calcination. This implies that the crystal

Fig. 5. XRD patterns of Ni/Y₂O₃ catalysts.

size of Y₂O₃ support does not influence the chemical environment of the impregnated nickel species. This observation is in contrast with other oxide supports, such as Al₂O₃, MgO or La₂O₃, which are readily to have strong association with Ni as shown by the increase in binding energy of nickel [45–47]. Fig. 6b shows that the binding energy of Y 3d_{5/2} for all these four calcined catalysts is around 156.2 eV, which is comparable with that of Y 3d_{5/2} for pure Y₂O₃ [48]. All of these results indicate that the chemical environmental of Y does not change with the crystal size of Y₂O₃ and the impregnated Ni does not react with Y₂O₃.

Table 2 shows that the Ni contents calculated based on XPS analysis are around 5 wt.%, which is higher than the values based on ICP analysis (3.6 wt.%). This is probably because ICP analysis gives an overall content while XPS gives the surface content. This result indicates that the surface Ni content is slightly higher than the overall Ni content in these Ni/Y₂O₃ catalysts. It is also noted from Table 2 that the specific surface areas of these catalysts are only slightly different, indicating that the crystal size of the support does not greatly influence the surface area of the corresponding catalyst.

It can be seen from Fig. 7 that all catalysts have a single reduction peak at about 385 °C, which agrees well with the reduction peak of pure NiO reported in literatures [49,50]. However, the association between nickel and support, such as Al₂O₃ significantly affects the reducibility of NiO, which usually results in the shift of its reduction peak [50–52]. Interestingly, the result of our study shows that no association has taken place between nickel and Y₂O₃ support, which is consistent with the observation from XPS analysis. Comparing Fig. 3 and Fig. 7, it can be seen that the peak assigned to the reduction of Y₂O₃ is not observed in the TPR profile of Ni/Y₂O₃ because the height of the reduction peak of Y₂O₃ (≈20) is so small that it is shadowed by the large reduction peak of NiO (≈500). This result provides further evidence that Y₂O₃ support is only partially reduced (as mentioned in Section 3.1). It can be further noticed from Fig. 7 that these reduction peaks, in terms

Fig. 6. XPS spectra of Ni/Y₂O₃ catalyst: (a) Ni 2p; (b) Y 3d.

of peak shape and intensity, are quite similar, indicating that the reducibility of nickel is not affected by the variation of the crystal sizes of Y₂O₃ supports.

The particle sizes of Ni on these four Ni/Y₂O₃ catalysts estimated from H₂-chemisorption are around 15, 13, 14 and 16 nm (Table 2), respectively, and they are comparable with the

Table 2
Textural characterizations of Ni/Y₂O₃ catalysts

Catalyst	Ni content (wt.%)		<i>S</i> _{BET} (m ² /g)	Ni particle size (nm)	Ni dispersion (%)
	Overall ^a	Surface ^b			
Ni/Y7	3.6 ± 0.1	5.1 ± 0.2	30	≈15	≈12
Ni/Y9	3.7 ± 0.1	5.2 ± 0.2	22	≈13	≈11
Ni/Y11	3.7 ± 0.1	4.9 ± 0.2	29	≈14	≈13
Ni/Y12	3.6 ± 0.1	4.8 ± 0.2	46	≈16	≈13

^a From ICP analysis.

^b From XPS analysis.

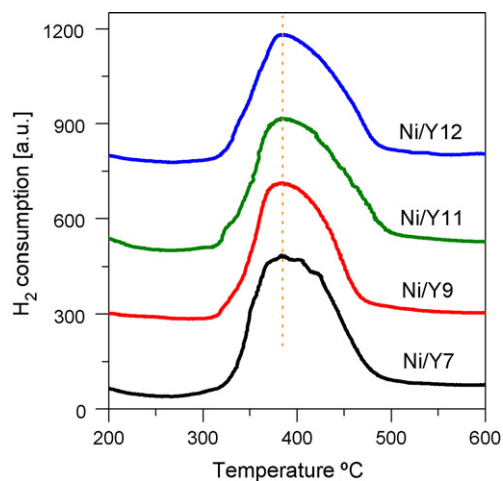


Fig. 7. TPR profiles of Ni/Y₂O₃ catalysts.

observation from TEM images. Table 2 also shows that the surface area of Ni/Y12 is larger than that of other catalysts, as the support-Y12 has larger surface area than other Y₂O₃, i.e. Y7, Y9 and Y11 (as shown in Table 1). It can be seen from Table 2 that the dispersions of Ni on these Ni/Y₂O₃ catalysts do not differ much, indicating that the dispersion of Ni is not affected by the crystal size of support. This result is quite different from that observed by Kugai et al. on the Ni-Rh/CeO₂ system [36]. They found that both the reducibility and dispersion of metals (Ni and Rh) were affected by the crystal size of CeO₂ support, which was attributed to the association between the metals and the CeO₂ support [36]. However, very little association between nickel and the support-Y₂O₃ has been observed in our study, probably because Y₂O₃ is thermodynamically more stable [53], and hence the reducibility and dispersion of Ni are not affected by the crystal size of Y₂O₃.

3.3. Activity test

Fig. 8 shows the catalytic performance (in terms of H₂ production rate) of these four Ni/Y₂O₃ catalysts on ethanol oxidative steam reforming reaction. Ni/Y12 catalyst gives the highest H₂ production rate at the temperature range of 500–750 °C while Ni/Y11, Ni/Y9 and Ni/Y7 give sequentially descending H₂ production rate. The difference in H₂ production rate between Ni/Y12 and Ni/Y7 is up to ~15%. It can be seen clearly that the catalytic performance of Ni/Y₂O₃ catalysts increases with the decrease in crystal size of Y₂O₃. A similar trend has also been observed by Kugai et al. [36] for the relationship between the catalytic performance of Ni-Rh/CeO₂ and the crystal size of the support-CeO₂, and they attributed this result to the fact that the metal dispersion had varied with the change of the crystal size of CeO₂ support. However, as mentioned earlier, the specific surface area of the catalyst, particle size and dispersion of nickel in our study do not differ greatly, and thus they may not be the key factors in causing the difference of the catalytic performance in the reaction system studied here. Furthermore, the difference in the catalytic performance of these catalysts is not related to the interaction between Ni and the different crystal sizes of Y₂O₃ since very

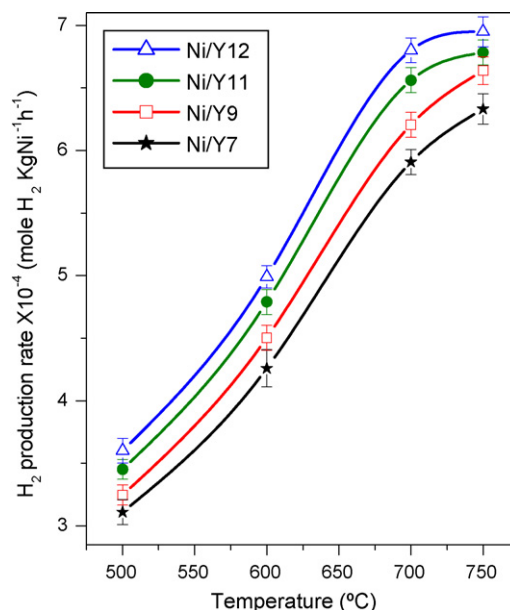


Fig. 8. Catalytic performance of Ni/Y₂O₃ catalysts (molar ratio of C₂H₅OH:H₂O:O₂ = 1:3:0.5; GHSV = 44 170 h⁻¹; carrier gas (N₂) = 30 ml/min).

little association of Ni and Y₂O₃ has been observed from all these catalysts based on the XPS and H₂-TPR results.

Interestingly, it is found that the order of mobility of surface oxygen species on Y₂O₃ supports is similar with that of the catalytic performance of the corresponding Ni/Y₂O₃ catalyst, suggesting that the surface oxygen mobility of Y₂O₃ support is the key factor in causing the difference in catalytic performance. The important role of mobile surface oxygen on a catalyst support has also been observed in other catalytic system [43,54,55]. For instance, it has been shown that Y₂O₃ or CeO₂ support is able to provide reactive oxygen species involved in CO oxidation reaction [54,55]. It is likely that the surface oxygen species provided by the support play an equally important role in the oxidative steam reforming reaction. Therefore, the difference in catalytic performance of these Ni/Y₂O₃ catalysts associated with the variation of the crystal size of Y₂O₃ supports can be attributed to the difference in the mobility of the surface oxygen species on Y₂O₃ support.

Fig. 9 shows that carbon forms during oxidative steam reforming of ethanol at the whole temperature range of 500–750 °C. It is also observed from Fig. 9 that the rate of carbon deposit is affected by the different crystal sizes of Y₂O₃, with less carbon deposited per unit time on the catalyst having smaller crystal size of Y₂O₃ support. The lower carbon deposit rate on the smaller crystal size of Y₂O₃ could also be attributed to the higher mobility of oxygen species on the surface of smaller Y₂O₃ nanocrystals since it has been reported that the carbon species are readily oxidized by the mobile surface oxygen species [56]. Furthermore, Fig. 9 shows that the carbon deposit is rather severe (around 400 mg C/g Cat/h) at 500 °C. When the reaction temperature increases over 600 °C, the rate of carbon deposit decreases obviously to 200 mg C/g Cat/h or less, probably because the carbon deposit is oxidized to CO and CO₂ at the elevated reaction temperature. These results indicate that the mobile surface oxygen species on Y₂O₃ support is

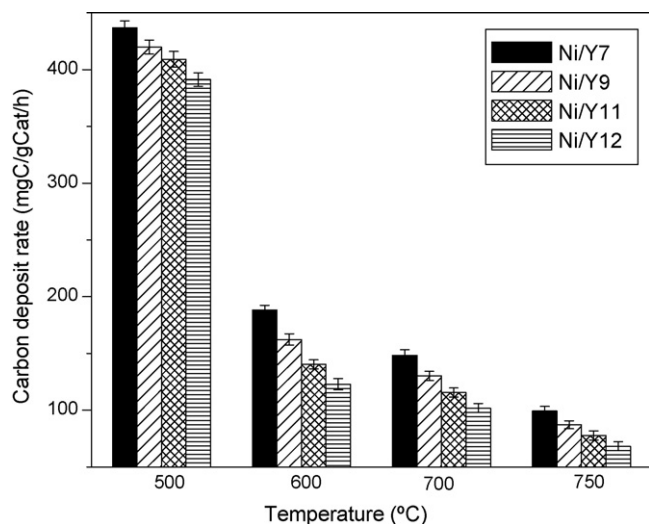


Fig. 9. Carbon deposit rate over Ni/Y₂O₃ catalysts during one-hour testing (molar ratio of C₂H₅OH:H₂O:O₂ = 1:3:0.5; GHSV = 44 170 h⁻¹; carrier gas (N₂) = 30 ml/min).

helpful in alleviating carbon deposit while higher reaction temperature is also important in overcoming the problem of carbon deposit.

Table 3 shows that H₂ selectivity is also affected by the crystal size of Y₂O₃. As shown in Table 3, Ni/Y12 achieves the highest H₂ selectivity at the whole temperature range while Ni/Y7 exhibits the lowest. This result could be explained by the fact that the mobile surface oxygen species on Y₂O₃ could selectively oxidize the carbon species [56] that adsorbed on the surface of catalysts instead of the hydrogen atom. This selective oxidation possibly enhances the dehydrogenation of ethanol or other hydrocarbon intermediates. As a consequence, the H₂ selectivity increases with the increase of the surface oxygen mobility of the support. Table 4 shows the carbon distribution in the product stream. As expected, the selectivities towards CO and CO₂ increase with the decrease of Y₂O₃ crystal size, while those towards CH₄ and other carbon-containing species decrease. This result indicates that the ability of catalyzing oxidation of carbon species increases with decreasing Y₂O₃ crystal size, which should be attributed to the increase of surface oxygen mobility of Y₂O₃. Table 5 shows the catalytic activity of pure Y₂O₃ (Y12). It is noted that H₂ selectivity is very low without the presence of Ni, indicating that the active component-Ni is inevitable for ethanol reforming reaction. It is also noted that CO and CO₂ were present in the product stream,

Table 4

Influence of Y₂O₃ support on selectivity towards CH₄, CO, CO₂ and others

Catalyst	Carbon distribution in product stream (%)			
	CH ₄	CO	CO ₂	C _{in other forms}
Ni/Y7	8.9	44.1	45.0	2.0
Ni/Y9	7.9	44.4	46.2	1.5
Ni/Y11	6.8	45.0	47.2	1.0
Ni/Y12	5.0	45.6	49.0	0.4

Reaction temperature: 700 °C; molar ratio of C₂H₅OH:H₂O:O₂ = 1:3:0.5; GHSV = 44 170 h⁻¹; carrier gas (N₂) = 30 ml/min.

indicating that the carbon species is catalytically oxidized over the Y₂O₃ catalyst. The mobile surface oxygen species is believed to play an important role in the oxidation reaction. Furthermore, no obvious catalyst deactivation was observed within the two-hour catalyst testing over the pure Y₂O₃, indicating that the surface mobile oxygen species can be replenished by the dissociated water and oxygen molecules. However, the selectivities toward CO and CO₂ are still quite low, probably because the Y₂O₃ catalyst support alone is not efficient in breaking down the carbon–carbon bond of the ethanol molecule.

Ni/Y12 has been selected as the catalyst to investigate the effect of oxygen in the feed stream on the catalyst activity for oxidative steam reforming of ethanol. Fig. 10 shows that the oxygen-to-ethanol ratio affects both the hydrogen production and the carbon deposit rate. It can be seen obviously that the rate of carbon deposit decreases rapidly while the hydrogen production rate slightly increases when a small amount of oxygen is introduced into the reaction system; the hydrogen production rate reaches a maximum at the O₂/ethanol molar ratio of 0.25, indicating that the oxidation of carbon species is prior to hydrogen oxidation. However, an excess amount of oxygen leads to the decrease of hydrogen production rate, probably because the excess oxygen increases the oxidation of hydrogen. Deluga et al. [19] reported a similar finding, i.e. too low C/O ratio reduced hydrogen production. Therefore, from the standpoint of hydrogen production and catalyst stability, the optimal oxygen-to-ethanol molar ratio is in the range of 0.25–0.5 for the oxidative steam reforming of ethanol.

The fractional conversion of ethanol as a function of W/F_{EtOH} at various temperatures is presented in Fig. 11. For a given value of W/F_{EtOH}, the ethanol conversion increased with increasing temperature, as expected. The conversions are about 50% or less due to the high ethanol feeding rate. Based on this

Table 3

Influence of Y₂O₃ support on H₂ selectivity

Catalyst	H ₂ selectivity (%)			
	500 °C	600 °C	700 °C	750 °C
Ni/Y7	42.3	53.7	64.9	74.5
Ni/Y9	44.6	56.1	65.9	77.6
Ni/Y11	46.0	58.2	68.1	78.2
Ni/Y12	47.2	60.1	71.4	79.8

Molar ratio of C₂H₅OH:H₂O:O₂ = 1:3:0.5; GHSV = 44 170 h⁻¹; carrier gas (N₂) = 30 ml/min.

Table 5

Activity of pure Y₂O₃ (Y12)

Temperature (°C)	H ₂ selectivity (%)	Carbon distribution in product stream (%)			
		CH ₄	CO	CO ₂	C _{in other forms}
500	4.1	3.5	3.8	9.2	83.5
600	5.1	7.1	4.5	12.2	76.2
700	6.8	6.2	6.3	12.9	74.6
750	9.3	5.7	13.4	13.6	67.3

Molar ratio of C₂H₅OH:H₂O:O₂ = 1:3:0.5; GHSV = 44 170 h⁻¹; carrier gas (N₂) = 30 ml/min.

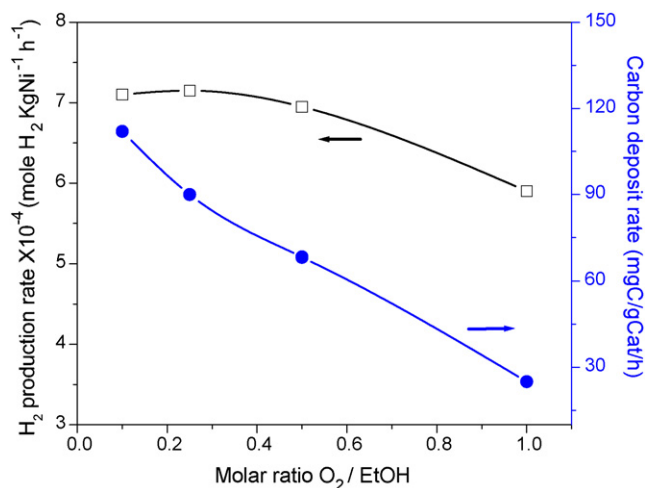


Fig. 10. Effect of O_2 /ethanol molar ratio on hydrogen production rate and carbon deposit rate over Ni/Y12 at 750 °C (molar ratio of $C_2H_5OH:H_2O = 1:3$; GHSV of water/ethanol = 39 260 h^{-1} ; carrier gas (N_2) = 30 ml/min).

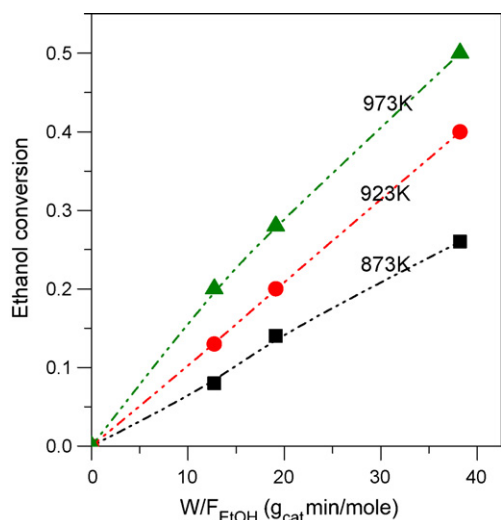


Fig. 11. Fractional conversions of ethanol as a function of W/F_{EtOH} at various temperatures over Ni/Y12 (molar ratio of $C_2H_5OH:H_2O:O_2 = 1:3:0.5$).

temperature dependence of the rate constants, activation energy is found to be around 5.8 kJ/mole. This value is consistent with that (7.04 kJ/mole) reported by Sun et al. [30]. It is also noted that this activation energy is much lower than that (16.88 kJ/mole) of Ni/Al_2O_3 [30], probably due to the influence of the high surface oxygen mobility of Y_2O_3 .

4. Conclusions

In summary, the morphology and crystal size of Y_2O_3 supports can be controlled using pH-controlled hydrothermal synthesis conditions. The dispersion and particle size of the impregnated metal-nickel species are not affected by the variation of the crystal size of Y_2O_3 . However, the crystal size of Y_2O_3 support affects the mobility of surface oxygen species on Y_2O_3 . The surface oxygen mobility has been identified to

play a crucial role in influencing the catalytic performance of Ni/Y_2O_3 catalyst on the oxidative steam reforming of ethanol.

Acknowledgement

The authors acknowledge financial support from National University of Singapore (Grant R-151-112 and R-179-112).

References

- [1] C.S. Song, Catal. Today 115 (2006) 2–32.
- [2] A. Patsoura, D.I. Kondarides, X.E. Verykios, Appl. Catal. B: Environ. 64 (2006) 171–179.
- [3] S. Ayabe, H. Omoto, T. Utaka, R. Kikuchi, K. Sasaki, Y. Teraoka, Appl. Catal. A: Gen. 241 (2003) 261–269.
- [4] J. Tong, Y. Matsumura, Appl. Catal. A: Gen. 286 (2005) 226–231.
- [5] J. Tong, L. Su, K. Haraya, H. Suda, Chem. Commun. (2006) 1142–1144.
- [6] J. Tong, Y. Matsumura, Chem. Commun. (2004) 2460–2461.
- [7] Z.Y. Zhong, Z.T. Xiong, L.F. Sun, J.Z. Luo, P. Chen, X. Wu, J. Lin, K.L. Tan, J. Phys. Chem. B 106 (2002) 9507–9513.
- [8] R.J. Farrauto, Appl. Catal. B: Environ. 56 (2005) 3–7.
- [9] C.S. Song, Catal. Today 77 (2002) 17–49.
- [10] V. Klouz, V. Fierro, P. Denton, H. Katz, J.P. Lisse, S. Bouvot-Mauduit, C. Mirodatos, J. Power Sources 105 (2002) 26–34.
- [11] D.K. Liguras, K. Goundani, X.E. Verykios, J. Power Sources 130 (2004) 30–37.
- [12] F. Marino, M. Boveri, G. Baronetti, M. Laborde, Int. J. Hydrogen Energy 26 (2001) 665–668.
- [13] A.N. Fatsikostas, D.I. Kondarides, X.E. Verykios, Chem. Commun. (2001) 851–852.
- [14] S. Freni, J. Power Sources 94 (2001) 14–19.
- [15] A. Haryanto, S. Fernando, N. Murali, S. Adhikari, Energy Fuels 19 (2005) 2098–2106.
- [16] J.P. Breen, R. Burch, H.M. Coleman, Appl. Catal. B: Environ. 39 (2002) 65–74.
- [17] F. Aupretre, C. Descorme, D. Duprez, Catal. Commun. 3 (2002) 263–267.
- [18] F. Aupretre, C. Descorme, D. Duprez, D. Casanave, D. Uzio, J. Catal. 233 (2005) 464–477.
- [19] G.A. Deluga, J.R. Salge, L.D. Schmidt, X.E. Verykios, Science 303 (2004) 993–997.
- [20] J. Llorca, P.R. de la Piscina, J. Sales, N. Homs, Chem. Commun. (2001) 641–642.
- [21] J. Llorca, N. Homs, J. Sales, J.L.G. Fierro, J. Catal. 222 (2004) 470–480.
- [22] F.J. Marino, E.G. Cerrella, S. Duhalde, M. Jobbogy, M.A. Laborde, Int. J. Hydrogen Energy 23 (1998) 1095–1101.
- [23] D.K. Liguras, D.I. Kondarides, X.E. Verykios, Appl. Catal. B: Environ. 43 (2003) 345–354.
- [24] J. Rasko, M. Domok, K. Baan, A. Erdohelyi, Appl. Catal. A: Gen. 299 (2006) 202–211.
- [25] J.J. Strohm, J. Zheng, C.S. Song, J. Catal. 238 (2006) 309–320.
- [26] S. Velu, N. Satoh, C.S. Gopinath, K. Suzuki, Catal. Lett. 82 (2002) 145–152.
- [27] Y. Yang, J. Ma, F. Wu, Int. J. Hydrogen Energy 31 (2006) 877–882.
- [28] D. Srinivas, C.V.V. Satyanarayana, H.S. Potdar, P. Ratnasamy, Appl. Catal. A: Gen. 246 (2003) 323–334.
- [29] V. Fierro, V. Klouz, O. Akdim, C. Mirodatos, Catal. Today 75 (2002) 141–144.
- [30] J. Sun, X. Qiu, F. Wu, W. Zhu, Int. J. Hydrogen Energy 30 (2005) 437–445.
- [31] J. Sun, X. Qiu, F. Wu, W. Zhu, W. Wang, S. Hao, Int. J. Hydrogen Energy 29 (2004) 1075–1081.
- [32] Y.Z. Yang, C.H. Chang, H. Idriss, Appl. Catal. B: Environ. 67 (2006) 217–222.
- [33] R.W. van den Brink, M. Krzan, M.M.R. Feijen-Jeurissen, R. Louw, P. Mulder, Appl. Catal. B: Environ. 24 (2000) 255–264.

- [34] P.E. Marti, M. Maciejewski, A. Baiker, *Appl. Catal. B: Environ.* 4 (1994) 225–235.
- [35] J. Guzman, A. Corma, *Chem. Commun.* (2005) 743–745.
- [36] J. Kugai, V. Subramani, C. Song, M.H. Engelhard, Y.H. Chin, *J. Catal.* 238 (2006) 430–440.
- [37] J. Zhang, Z. Liu, J. Lin, J. Fang, *Cryst. Growth Des.* 5 (2005) 1527–1530.
- [38] X. Wang, Y. Li, *Chem. Eur. J.* 9 (2003) 5627–5635.
- [39] X. Wang, X. Sun, D. Yu, B. Zou, Y. Li, *Adv. Mater.* 15 (2003) 1442–1445.
- [40] B. Ita, P. Murugavel, V. Ponnambalam, A.R. Raju, *Proc. Indian Acad. Sci.* 115 (2003) 519–524.
- [41] F.B. Passos, E.R. Oliveira, L.V. Matto, F.B. Noronha, *Catal. Lett.* 110 (2006) 261–267.
- [42] S.S. Lin, C.L. Chen, D.J. Chang, C.C. Chen, *Water Res.* 36 (2002) 3009–3014.
- [43] E. Mamontov, T. Egami, *J. Phys. Chem. B* 104 (2000) 11110–11116.
- [44] S. Velu, K. Suzuki, M. Vijayaraj, S. Barman, C.S. Gopinath, *Appl. Catal. B: Environ.* 55 (2005) 287–299.
- [45] J.C.D. Jesus, I. Gonzalez, A. Quevedo, T. Puerta, *J. Mol. Catal. A: Chem.* 228 (2005) 283–291.
- [46] J. Requies, M.A. Cabrero, V.L. Barrio, M.B. Guemez, J.F. Cambra, P.L. Arias, F.J. Perez-Alonso, M. Ojeda, M.A. Pena, J.L.G. Fierro, *Appl. Catal. A: Gen.* 289 (2005) 214–223.
- [47] E. Ruckenstein, Y.H. Hu, *J. Catal.* 161 (1996) 55–61.
- [48] M.D. Ulrich, J.E. Rowe, D. Niu, G.N. Parsons, *J. Vac. Sci. Technol. B: Microelectron.* 21 (2003) 1792–1797.
- [49] W. Shan, M. Luo, P. Ying, W. Shen, C. Li, *Appl. Catal. A: Gen.* 246 (2003) 1–6.
- [50] G. Li, L. Hu, J.M. Hill, *Appl. Catal. A: Gen.* 301 (2006) 16–24.
- [51] E. Ruckenstein, Y.H. Hu, *J. Catal.* 162 (1996) 230–238.
- [52] Z.X. Cheng, X.G. Zhao, J.L. Li, Q.M. Zhu, *Appl. Catal. A: Gen.* 205 (2001) 31–36.
- [53] M. Pospisil, P. Kanokova, *J. Therm. Anal. Calorim.* 58 (1999) 77–88.
- [54] J. Guzman, S. Carrettin, A. Corma, *J. Am. Chem. Soc.* 127 (2005) 3286–3287.
- [55] J. Guzman, S. Carrettin, J.C.F. Gonzalez, Y. Hao, B.C. Gates, A. Corma, *Angew. Chem. Int. Ed.* 44 (2005) 4778–4781.
- [56] M.M. Schubert, S. Hackenberg, A.C. van Veen, M. Muhler, V. Plzak, R.J. Behm, *J. Catal.* 197 (2001) 113–122.